

## Finescale Vertical Structure of the Upwelling System off Southern Peru as Observed from Glider Data

ALICE PIETRI, PIERRE TESTOR, AND VINCENT ECHEVIN

*LOCEAN, Paris, France*

ALEXIS CHAIGNEAU

*LEGOS-OMP, Toulouse, France*

LAURENT MORTIER

*LOCEAN, Paris, France*

GERARD ELDIN

*LEGOS-OMP, Toulouse, France*

CARMEN GRADOS

*IMARPE, Chucuito-Callao, Peru*

(Manuscript received 6 February 2012, in final form 30 November 2012)

### ABSTRACT

The upwelling system off southern Peru has been observed using an autonomous underwater vehicle (a Slocum glider) during October–November 2008. Nine cross-front sections have been carried out across an intense upwelling cell near 14°S. During almost two months, profiles of temperature, salinity, and fluorescence were collected at less than 1-km resolution, between the surface and 200-m depth. Estimates of alongshore absolute geostrophic velocities were inferred from the density field and the glider drift between two surfacings. In the frontal region, salinity and biogeochemical fields displayed cross-shore submesoscale filamentary structures throughout the mission. Those features presented a width of 10–20 km, a vertical extent of ~150 m, and appeared to propagate toward the shore. They were steeper than isopycnals and kept an aspect ratio close to  $f/N$ , the inverse of the Prandtl ratio. These filamentary structures may be interpreted mainly as a manifestation of submesoscale turbulence through stirring of the salinity gradients by the mesoscale eddy field. However, meandering of the front or cross-frontal wind-driven instabilities could also play a role in inducing vertical velocities.

### 1. Introduction

The Peruvian coast features the northern Humboldt Current System (NHCS), one of the four major eastern boundary current systems in the World Ocean. In this region, the presence of relatively strong and sustained atmospheric coastal wind jets (Enfield 1981) causes offshore Ekman surface flows driving intense coastal upwelling cells (Strub et al. 1998). This upwelling regime

brings cold, nutrient-rich subsurface waters to the surface, resulting in a high primary productivity and a rich ecosystem (Chavez et al. 2008).

The coastal circulation in the NHCS is mainly characterized by the relatively strong equatorward coastal current, the Peru coastal current (PCC), which flows alongshore at a speed of ~15 cm s<sup>-1</sup> (Huyer et al. 1991), and the subsurface poleward Peru–Chile undercurrent (PCUC) trapped along the continental slope (50–100 km from the coast) and centered at around 150–200-m depth, characterized by a maximum velocity of ~15 cm s<sup>-1</sup> (Huyer 1980). The upwelling front, which separates the relatively cold and fresh coastal water from the warmer

Corresponding author address: Alice Pietri, LOCEAN, 4 Place Jussieu, Case 100, 75252 Paris CEDEX 05, France.  
E-mail: alice.pietri@locean-ipsl.upmc.fr

and saltier offshore subtropical water, is characterized by strong horizontal density gradients and vertical shear in alongshore velocities making it baroclinically unstable (Penven et al. 2005; Echevin et al. 2011). Instabilities of the current system generate meanders and mesoscale eddies characterized by horizontal scales of  $\sim$ 50–100 km, which propagate westward and export coastal water properties to the offshore ocean (Chaigneau et al. 2008a, 2009).

At smaller spatial scales ( $\sim$ 1–10 km), submesoscale turbulence is also highly energetic in upwelling regions (Paduan and Niiler 1990). Recent observations (Pallás-Sanz et al. 2010; Johnston et al. 2011) as well as high-resolution modeling studies (Capet et al. 2008a,b; McWilliams et al. 2009) have shown that submesoscale features can arise through surface frontogenesis and through interactions between the upwelling front and the Ekman currents. Such processes could be particularly important for the functioning of the upwelling ecosystem since they are associated with intense vertical velocities (Capet et al. 2008b) that allow an important exchange of heat, nutrients, and biomass between the productive euphotic surface layer and the subsurface layer. Filamentary submesoscale structures can also arise through stirring of thermohaline gradients by mesoscale turbulence (Smith and Ferrari 2009). However, relatively little is known today about submesoscale processes and their impact on the dynamics and ecosystem, because of limitations in instrumental sampling and spatial resolution in models (Capet et al. 2008a).

In this paper, we characterize thermohaline features observed in the vicinity of the intense upwelling front located off Peru near Pisco ( $14^{\circ}$ S) and analyze the potential mechanisms leading to the formation of such features. Our analysis is based on a dataset of many variables acquired at a very high spatiotemporal resolution across the upwelling front, collected with an autonomous underwater vehicle (glider) during austral spring 2008.

After describing the observational dataset (section 2), we present an estimation of “absolute geostrophic velocities” using glider data (section 3) and outline the general structure of the upwelling area (section 4). In section 5 we characterize the fine spatial scales of the *T*–*S* intrusions observed in the frontal region and discuss the relevant driving mechanisms that could explain the observed submesoscale activity.

## 2. Data and methods

The Peruvian component of the Variability of American Monsoon Systems (VAMOS) Ocean–Cloud–Atmosphere–Land Study (VOCALS) Regional Experiment

(VOCALS-Rex, <http://www.eol.ucar.edu/projects/vocals/rex.html>) was conducted with the main purpose of documenting the mesoscale oceanic variability and its relation to the atmospheric coastal jet (Wood et al. 2010) and to provide a comprehensive description of the oceanic and atmospheric interaction and variability off southern Peru, between Callao ( $12^{\circ}$ S,  $77^{\circ}$ W) and San Juan ( $15^{\circ}$ S,  $76^{\circ}$ W).

A cruise operated by the R/V *Jose Olaya* [Instituto del Mar del Peru (IMARPE)] was devoted to an extensive sampling, at mesoscale, of the physical and biogeochemical oceanic features between Callao and San Juan with a Seabird SBE911 + conductivity–temperature–depth (CTD) probe, equipped with dissolved oxygen sensor, fluorometer, and a carousel for water samples. The R/V *Jose Olaya* carried out 14 cross-shore sections of  $\sim$ 100 km to  $\sim$ 300 km length with a total of 119 CTD profiles from 3 to 17 October (Wood et al. 2010). During the whole cruise, direct current data were obtained from an OS-75 RD Instruments vessel-mounted acoustic Doppler current profiler (ADCP). Vertical profiles of horizontal velocities were recorded as 10-min averages with a vertical resolution of 8 m; the first depth bin was centered at 16-m depth, and the range of the instrument exceeded 600 m most of the time. Data was processed using the Common Ocean Data Access System (CODAS) software developed at the University of Hawaii (<http://currents.soest.hawaii.edu>).

In this framework, a glider was deployed on 3 October and recovered, in emergency because of a mechanical failure, on 24 November 2008. The glider was deployed at  $14.01^{\circ}$ S,  $76.55^{\circ}$ W about 30 km off the Paracas Peninsula, south of Pisco ( $14^{\circ}$ S), a well-known strong upwelling cell (Strub et al. 1998) and a propitious region for the formation of mesoscale eddies (Chaigneau et al. 2008a, 2009). The objective was to determine the finescale structure of the upwelling plume and front as well as their temporal variability.

Gliders (Davis et al. 2002; Rudnick et al. 2004; Testor et al. 2010) are autonomous, buoyancy-propelled, fixed-wing underwater vehicles characterized by a small size (about 1.5 m long and 20 cm in diameter) and a weight of around 50 kg ( $\sim$ 200 g in seawater) equipped with miniaturized oceanographic sensors. Without a propeller, they move through the ocean following a saw-tooth pattern between the surface and a programmed nominal depth (typically 200 m or 1000 m) by changing their buoyancy and using lift on wings to convert induced vertical velocities into a forward motion. They achieve vertical speeds of  $10\text{--}20\text{ cm s}^{-1}$  and forward speeds of  $20\text{--}40\text{ cm s}^{-1}$ . They periodically surface for GPS positioning and bidirectional data transmission through the Iridium satellite system. Under water, they use dead

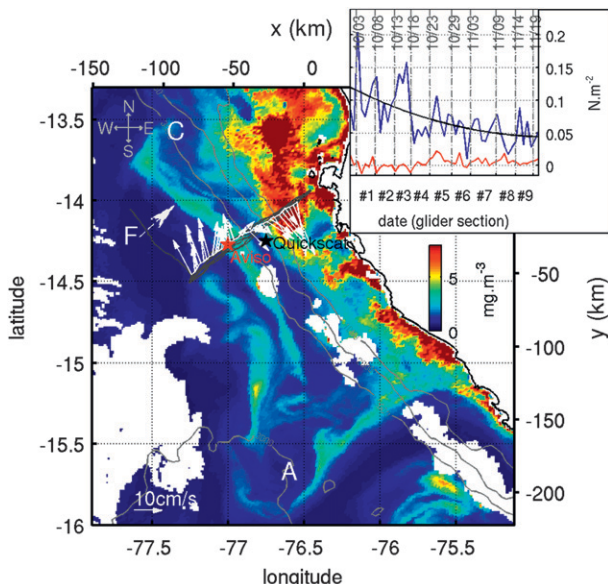


FIG. 1. Surface chlorophyll concentration ( $\text{mg m}^{-3}$ ) from the Moderate Resolution Imaging Spectroradiometer (Modis) (14–16 Nov 2008). Gray lines indicate glider trajectories. The white line indicates the glider trajectory between 14 and 19 Nov (section #9) and white arrows mark 0–200 m depth-averaged water velocities. Location of estimated QuikSCAT windstress is marked by a black star and location of the estimated surface current from AVISO by a red star. Labels denote the location of a cyclonic eddy (C), an anti-cyclonic eddy (A) and a filament (F). Inset: Quikscat windstress components along (red) and perpendicular (blue) to the glider section.

reckoning with attitude sensors (heading, pitch, and roll). They follow dive/ascent angles of  $\pm 25^\circ$  to the surface. The angles are much steeper than typical isopycnal slopes, so the collected profiles can be considered as vertical profiles in a “shallow water” framework. During VOCALS-REx we used a Slocum glider developed by Webb Research Corporation, fitted with pressure, conductivity, and temperature sensors (unpumped Seabird SBE-41CP), and a turbidity and fluorescence FLNTU “puck” from Wetlabs.

Nine sections perpendicular to the continental slope from  $\sim 10$  km off the coast to  $\sim 100$  km offshore were carried out by the glider between 3 October and 24 November 2008 (Fig. 1). During this 7-week period of operation, the glider acquired more than 1300 profiles, from the surface down to a nominal depth of 200 m. Glider data are collected with a typical vertical resolution of about 1–2 dbar and were interpolated onto a regular 1 dbar vertical grid. For each cross-shore section, about 130 profiles (more than 1 profile/km) were collected. Glider data also allows estimating the depth-averaged current in the upper layer (0–200 m) and between two surfacings, using the difference between underwater dead reckoning and the GPS fixes at the surface. Each profile GPS location

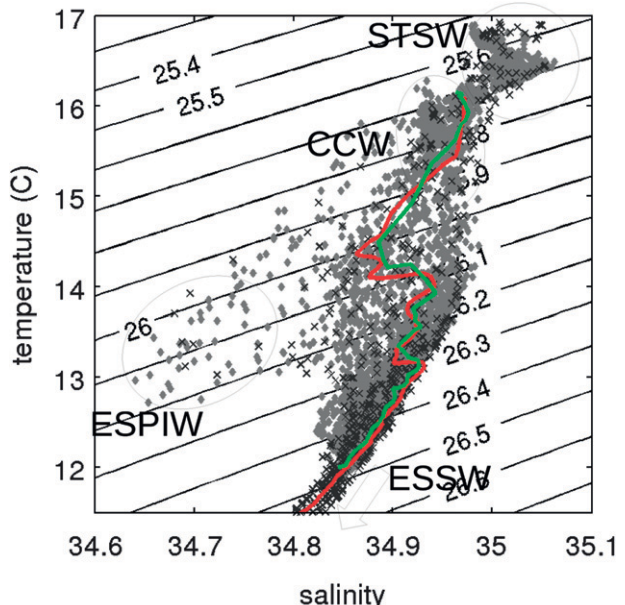


FIG. 2. The  $\Theta$ -S diagram from glider section 2 data (diamonds) and from R/V *Olaya* CTD data along the glider track (crosses). Green and red lines indicate the closest profiles (3.8 km and 1 h 30 min) from the glider and the ship, respectively.

was projected onto a cross-shore straight line in order to obtain a strictly two-dimensional dataset.

Shipboard CTD measurements acquired in the vicinity of the glider during its deployment are used to calibrate the glider salinity data. First, a general offset of  $7 \times 10^{-4} \text{ S m}^{-1}$  in conductivity was applied so as to obtain similar salinities in both datasets at 200-m depth. Second, thermal inertia and time responses were corrected by aligning temperature and conductivity data for the computation of salinity. We used a lagged temperature  $T_c$ :

$$T_c = T - \tau_c \frac{\delta T}{\delta t},$$

where  $T$  is the temperature time series, and  $\tau_c$  an empirical time constant, to compute salinity values that are corrected from all these effects together, which are important essentially within the thermocline where the vertical temperature gradients are high.

Comparisons between the glider CTD data and the pumped shipborne CTD data on the  $\Theta$ -S diagram allowed us to determine the optimal value for  $\tau_c$ . With  $\tau_c = 3$  s, the slopes in pumped and unpumped data corresponding to the thermocline are similar, and the difference above and below the thermocline are negligible. The two datasets are in very good agreement considering the spatial differences and temporal delays between the glider and the ship measurements (Fig. 2).

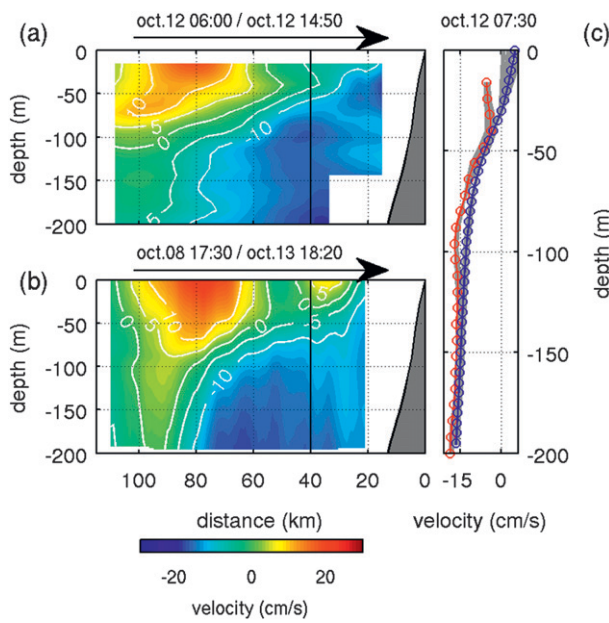


FIG. 3. (a) ADCP current and (b) absolute geostrophic current from glider section #2, perpendicular to the glider section. The meeting point between the glider and the ship is indicated by a vertical black line. (c) Velocity profiles from ADCP data (red line) and from glider data (blue line) at the meeting point. Profiles around the meeting point (within 10 km and 15 h for the glider and 10 km and 1 h for the R/V *Olaya*) are indicated in gray.

### 3. “Absolute” geostrophic velocities

The density and the depth-averaged current data derived from the glider’s position can be used to estimate profiles of absolute geostrophic velocity perpendicular to the sections, as in Gourdeau et al. (2008). However, the underlying hypothesis of geostrophic flow must be carefully evaluated. R/V *Olaya* shipboard ADCP measurements carried out along the glider section on 12 October show a northward surface current flowing at  $\sim 15 \text{ cm s}^{-1}$  and a southward subsurface current flowing at  $\sim -10 \text{ cm s}^{-1}$  (Fig. 3a). The order of magnitude for horizontal currents is thus  $U \sim 10 - 20 \text{ cm s}^{-1}$  for an associated length scale  $L \sim 50 - 100 \text{ km}$ , yielding a Rossby number,  $\text{Ro} = U/fL \sim 0.03 - 0.13$ , typical of the upwelling system. The flow can thus be considered as mainly geostrophic at mesoscale. Furthermore, as the wind is mostly perpendicular to the glider track (see inset in Fig. 1), Ekman flow contributes little to the alongshore current. Thus, the depth-averaged current perpendicular to the glider section can provide a good estimate for the reference velocity to geostrophic computations.

At  $14^\circ\text{S}$  the inertial period is of  $\sim 50 \text{ h}$  and inertial currents in the study region are among the weakest of the World Ocean (Chaigneau et al. 2008b). The Rossby radius of deformation along an averaged section ranges

from 15 km in the coastal area to 40 km offshore. The density field as measured by the glider is characterized by high frequency variations on top of mesoscale patterns. To filter the high frequency variations while conserving the mesoscale gradients, a triangular moving average of 30 km horizontally (corresponding to  $\sim 35 \text{ h}$  at the speed of the glider) was applied to the density field and the depth-averaged currents. The thermal wind balance was then integrated between the surface and 200 m, the depth-averaged current perpendicular to the section providing a reference velocity. We tested that this filtering gives similar results than just considering profiles distant from a Rossby radius. The mean difference between the velocity inferred from the filtered fields and the one inferred from distant profiles is only  $\sim 1.8 \text{ cm s}^{-1}$ . Note that both methods would certainly induce a bias since two glider profiles 40 km apart are also two days apart, which is very close to the inertial period. For the sake of simplicity, we use the alongshore velocity computed with smoothed fields as an estimate of “absolute geostrophic velocity,” keeping in mind that the uncertainty on these estimates can reach  $\sim 1 - 2 \text{ cm s}^{-1}$ .

On all nine sections, this mesoscale absolute alongshore circulation is characterized by an offshore surface equatorward current associated with the PCC and a nearshore subsurface poleward undercurrent related to the PCUC. The core of the PCC centered at 80 km ( $\pm 10 \text{ km}$ ) from the coast, shows a maximum speed of  $\sim 30 \text{ cm s}^{-1}$ , an average width of  $\sim 50 \text{ km}$ , and a vertical extent of  $\sim 100 \text{ m}$ , slightly stronger and deeper than observed previously (Brink et al. 1983; Huyer et al. 1991). Transport of the PCC was computed from the equatorward velocities derived from the glider. It ranges between 0.4 Sv and 1.3 Sv ( $\text{Sv} \equiv 10^6 \text{ m}^3 \text{ s}^{-1}$ ) with an average transport of 0.8 Sv. Previous observations of the PCUC in the region indicate a mean speed of  $10 \text{ cm s}^{-1}$ , the maximum velocity being centered near the continental slope at  $\sim 150 \text{ m}$  depth, and a confinement within 60 km from the coast (Huyer et al. 1991). Even though the glider dives were not deep enough to sample the PCUC entirely over the vertical, geostrophic estimates are consistent with these previous observations. Indeed, one can observe the PCUC with a maximum speed of  $\sim 15 \text{ cm s}^{-1}$  at 150-m depth and a width ranging from 50 to 80 km at 200-m depth (Fig. 3b).

The R/V *Olaya* shipboard ADCP measurements allow us to validate these computations (Fig. 3a). The ship and the glider met each other at 40 km from the coast on 12 October (black vertical line on Figs. 3a and 3b). Velocity profiles at the meeting point are correlated with a coefficient of 0.9, a mean difference of  $1.4 \text{ cm s}^{-1}$ , and rms of  $1.9 \text{ cm s}^{-1}$  (Fig. 3c). However at  $\sim 100 \text{ m}$  there is a maximum difference between the profiles of  $\sim 4 \text{ cm s}^{-1}$

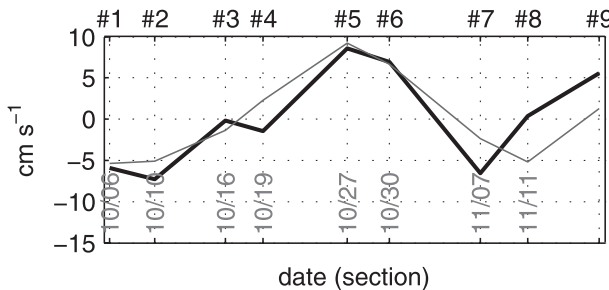


FIG. 4. Surface geostrophic velocity anomaly at 14.27°S, 77°W derived from AVISO (thin gray line) and from the glider data (bold black line). Glider surface velocity anomaly was averaged around the AVISO data point ( $\pm 20$  km, 0–10-m depth).

indicating that ageostrophic motion could be important. Despite the fact that the glider section was completed in five days and the ADCP section was completed in only one day, both display a rather similar vertical structure at the mesoscale and have velocities of the same order of magnitude (Figs. 3a and 3b). There are, however, some differences between the two estimates of the currents along this section. They could be due to uncertainties in the ADCP measurements [16-m resolution along the vertical and 1–5  $\text{cm s}^{-1}$  accuracy, Fischer and Visbeck (1993)], result from the less synoptic character of the glider measurements, or being linked with ageostrophic velocities. Note the surface positive velocity near  $\sim 30$ –50 km from the shore present only in the glider section (Fig. 3b), the subsurface local maximum near  $\sim 90$ –110 km from the shore and at  $\sim 60$  m deep in the ADCP data (Fig. 3a), and the position of the sheared zone between the equatorward and the poleward current within 100–150 m depth and  $\sim 60$ –90 km from the shore (Fig. 3).

The temporal variability of the surface geostrophic current measured during the glider mission can also be compared with independent velocity measurements such as those derived from satellite altimetry. Anomalies of the surface current from glider and Archiving, Validation, and Interpretation of Satellite Oceanographic (AVISO) data (<http://www.aviso.oceanobs.com/>) data have been computed at 14.27°S, 77°W near the mean position of the PCC core observed on each glider section (Fig. 4). The two time series are in very good agreement with a correlation coefficient of 0.8, thereby indicating that the subinertial temporal variability of the surface current is captured in the glider data.

#### 4. Cross-shore vertical structure of the upwelling system

##### a. Water masses

The  $\Theta$ –S diagram derived from the salinity and temperature measurements of the glider along section #2

and from the *Olaya* CTD along the same section are superimposed in Fig. 2. From both datasets, four main water masses can be identified in the upper 200 m:

- the cold coastal water (CCW) characterized by a relatively high salinity (34.9 to 35) and low temperature (15°–16°C) at the surface and near the coast;
- the subtropical surface water (STSW) characterized by a relatively high salinity (35 to 35.1) and temperature (16°–18°C) offshore in the surface layer;
- the eastern South Pacific Intermediate Water (ESPIW) (Schneider et al. 2003) characterized by a very low salinity (34.6–34.8) at the base of the thermocline and originating from the subantarctic region; and
- the equatorial subsurface water (ESSW) (0°–12°C and 34.7–34.9) observed below 100-m depth.

Figure 5 shows the salinity and temperature CTD section carried out by the R/V *Olaya* along with the glider section #2 superimposed, highlighting the difference in horizontal sampling between the vessel and the glider data. Three different regions can be identified:

- a cold *coastal region* (0–30 km from shore) where the upwelling takes place,
- a *transition zone* (30–90 km) with strong horizontal gradients in the surface layer associated with the upwelling front, and
- a warmer and saltier *offshore region* (90–180 km) corresponding to the open ocean.

Figure 5 shows that the glider mainly occupied the transition zone providing high resolution data between the coastal region and the offshore region. The same water masses can be identified in both datasets. Note in particular, the fresh ESPIW, which is observed on the salinity field below the thermocline (at  $x \sim 80$  km and  $x \sim 140$  km). The transition zone appears as a region of particularly strong horizontal salinity gradients where the ESPIW, the CCW and the STSW can mix (Fig. 5b).

Figure 6, showing the nine consecutive glider sections, provides an overview of the upwelling front variability during the whole experiment. The temperature field (Fig. 6a) exhibits the cold coastal region, the warmer offshore region, and the transition zone as expected for an upwelling area and observed in the ship's profile data. In the offshore region, the surface temperature gets warmer from 3 October ( $\sim 16^\circ\text{C}$ ) to 19 November ( $\sim 18^\circ\text{C}$ ), and the mixed layer tends to stratify. In contrast, surface temperature remains cold ( $\sim 15^\circ\text{C}$ ) close to the coast. The salinity field (Fig. 6b) displays small-scale slanted structures spaced by  $\sim 20$  km in the transition zone, which are not observed from the ship's CTD profiles because of too coarse horizontal sampling.

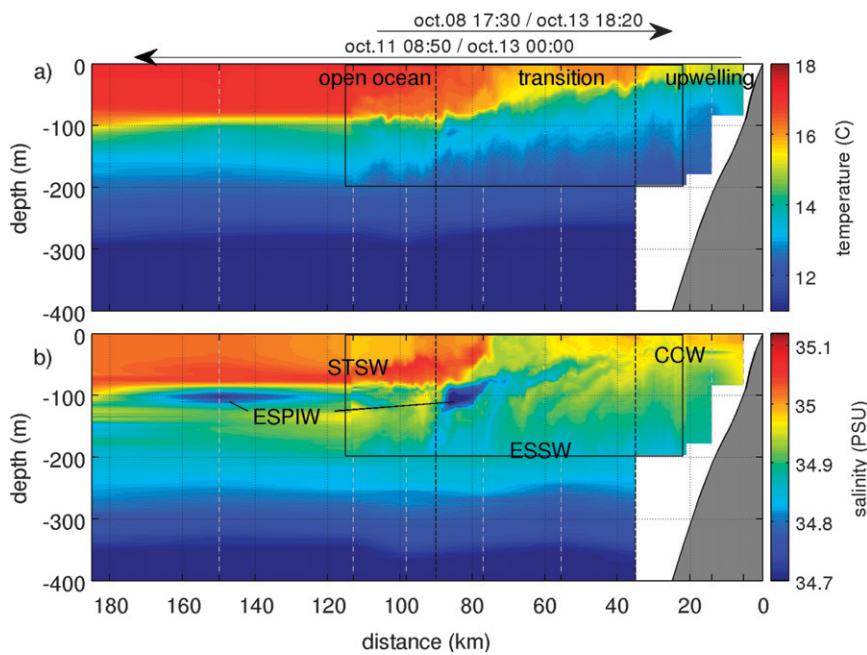


FIG. 5. Vertical sections of (a) potential temperature and (b) salinity carried out from R/V *Olaya* between 11 and 13 Oct along a section contiguous to the glider sections. The glider section #2 (8–13 Oct) is superimposed in the black rectangle. Three regions (offshore, transition, and coastal) are delimited by black dashed lines. Ship CTD casts are indicated with thin gray-dashed lines.

### b. Salinity tongues

The ESPIW, the ESSW, and the CCW are distributed along alternating tongues of relatively high and low salinity (Fig. 7). These tongues of high ( $\sim 34.9 - 35$  psu) and low ( $\sim 34.75 - 34.85$  psu) salinity extend from  $z \sim 30$  m to at least  $z \sim 200$  m and between  $x \sim 30$  km and  $x \sim 100$  km. They have a cross-isopycnal extension and become steeper closer to the coast (black dashed lines in Fig. 7). For each feature that can be identified visually on the sections, the horizontal position of the local salinity minima (maxima) at 120-m and 80-m depth in a  $\sim 30$ -km-wide spatial window centered on the tongue at 100-m depth was used to derive its cross-shore slope. The computed slopes vary from 0.2% to 1.5%. Noteworthy, each glider section exhibits approximately two to three tongues of fresh (saltier) water (Fig. 6b) with an average horizontal width of  $\sim 10$  km. Their horizontal extent is narrower near the surface (2–5 km at 50–100-m depth) and larger (up to 10 km) at depths greater than 100 m. Horizontal gaps between the fresh tongues range from 10 km (near 50–100-m depth) to 40 km (near 100–150-m depth). Below  $\sim 150$  m in the ESSW, horizontal salinity gradients are weaker and the fresh tongues are less visible.

### c. Fluorescence (Chlorophyll *a*)

Fluorescence is an indicator of chlorophyll concentration and is generally considered as a proxy of phytoplankton

biomass under nonlimiting environmental conditions. Indeed, the ratio between the chlorophyll concentration and phytoplanktonic biomass can vary significantly according to light, nutrients, and temperature (Behrenfeld and Boss 2006). Besides conversion from volts/counts to actual pigment concentration requires careful calibration of the fluorescence data with the filtration of water samples and their analysis. The fluorometer on board the glider was not calibrated in such a way, and the fluorescence data is used here only qualitatively.

The fluorescence field shown in Fig. 6c exhibits high concentrations in the mixed layer between  $\sim 20$  and  $\sim 80$  km from the coast. A diurnal cycle showing decreases of chlorophyll during daytime because of quenching can be observed in the first 10 m, particularly in the offshore region (see sections #1 at 100 km, #2 at 75 and 95 km, #3 at 85 and 105 km, #4 at 80 and 100 km, #5 at 90 and 110 km, #6 at 105 km, #7 at 80 and 100 km, #8 at 80 and 100 km, and #9 at 90 km). In the coastal and transition regions subsurface chlorophyll patterns can indicate both local biological activity and the presence of upwelled and downwelled water. Tongues of high fluorescence extending well below the euphotic layer are also visible below the mixed layer. Significant patches with concentrations greater than 1% of the surface maximum values can be observed as deep as 150 m in the transition zone on each section. More particularly, they can reach values up to 5% below 100 m depth in

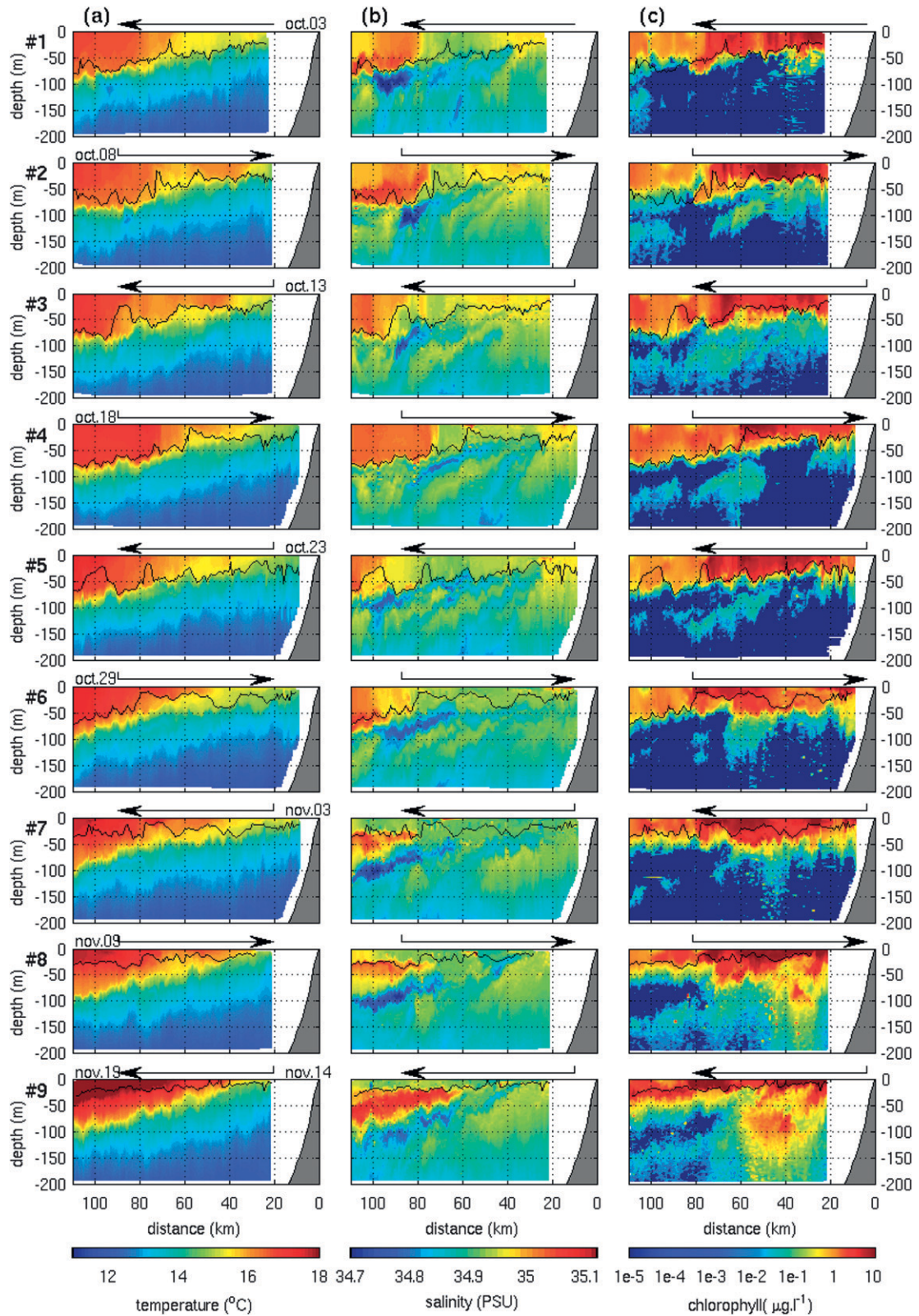


FIG. 6. (a) Potential temperature ( $^{\circ}\text{C}$ ), (b) salinity (psu), and (c) chlorophyll (concentration,  $\mu\text{g L}^{-1}$ ) for all glider sections. The mixed layer depth estimated from a  $0.4^{\circ}\text{C}$  temperature difference criteria is marked by a dark gray line.

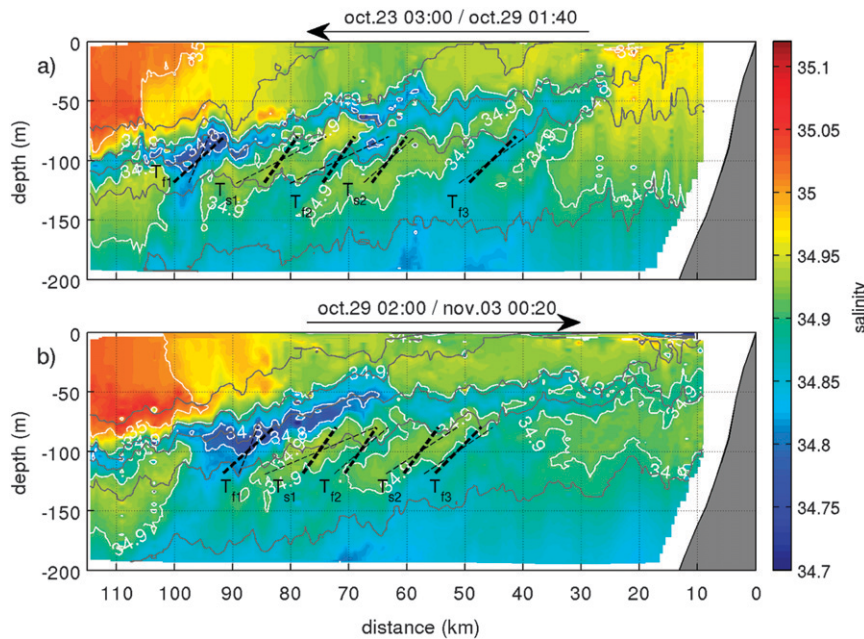


FIG. 7. Salinity from glider section (a) #5 and (b) #6 (color coded); salinity contours (white) and density contours (gray) are overlaid. The slopes of the salinity structures are marked by thin dashed lines (calculated from the minimum of salinity at 120 m and 80-m depth). Bold dashed lines mark  $f/N$  slopes, with  $N$  calculated at 100-m depth.

sections #7–9. Light intensity being very low in this depth range, it is unlikely that phytoplankton develops locally. Such high concentrations can result from enhanced intracellular pigmentation of planktonic cells due to the lack of light and nutrients or from downward transport of phytoplankton generated in the surface layer and decaying at depth, as suggested by the continuity of these tongues between the surface and 100–150-m depth. Note that locally developed phytoplankton bloom can also be advected by the horizontal current field and not necessarily correspond to vertical fluxes (Viúdez and Claret 2009). However, the glider sections (particularly sections #2 to #5) show that tongues of relatively high fluorescence located below the euphotic layer are collocated with tongues of relatively high ( $\sim 34.95$ ) salinity. Reciprocally, low chlorophyll concentrations are collocated with fresh tongues. This suggests that the same dynamical process may be responsible for the structures on both fields.

#### d. Coastward displacement of the salinity anomalies

Salinity tongues have been observed in the nine glider sections. Some of the tongues seem similar from one section to the next. Furthermore, these persistent features seem to propagate coastward while getting steeper (Fig. 6b). Figure 7 shows an example of this coastward displacement between glider sections #5 and #6 where very similar features can be identified but at different

positions. On glider section #5 (Fig. 7a) between  $\sim 60$  and  $\sim 100$  km from the coast at  $\sim 100$ -m depth, two tongues of high salinity ( $T_{s1}$  and  $T_{s2}$ ) and two tongues of low salinity ( $T_{f1}$  and  $T_{f2}$ ) can be observed. Similar structures can be found on glider section #6  $\sim 5$  days later, between  $\sim 50$  and  $\sim 90$  km, thus closer to the coast (Fig. 7b).

Figure 8 shows the time evolution of the salinity at 120-m depth for the whole deployment. Local minima (respectively maxima) were matched with the features observed on the vertical sections to highlight their displacement

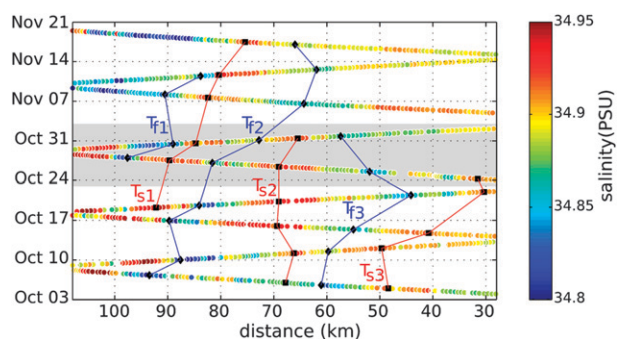


FIG. 8. Hovmöller diagram of salinity at 120 m. Black squares and diamonds indicate the position of local maxima and minima, respectively, representative of each salinity features observed on the vertical sections. Blue (red) lines represent the displacement of the anomalously fresh (saline) features with time. The gray area highlights the period including the glider sections #5 and #6 presented in Fig. 7.

from one section to the next (see Fig. 7 for glider sections #5 and #6). This method is obviously subjective but it gives a general idea of the cross-shore displacement of the structures. The displacement of each salinity extremum from one section to the next ranges from  $\sim -0.9$  to  $\sim 4.2 \text{ cm s}^{-1}$  with an average velocity of  $\sim 0.8 \text{ cm s}^{-1}$ . The contrast between the salinity tongues was best observed at 120 m but a similar range of velocities was obtained at other depths between 80 and 150 m (not shown).

This coastal displacement between 80 and 150 m could be related with a cross-shore return flow compensating the offshore (seaward) Ekman surface transport (Smith 1981; Lentz and Chapman 2004). A rough estimate of the return flow can be computed as follows using a mass budget. Quick Scatterometer (QuikSCAT) satellite wind stress  $\tau^y$  from the Center for Satellite Exploitation and Research (CERSAT, <http://www.ifremer.fr/cersat>), projected perpendicularly to the glider section is on the order of  $6.8 \times 10^{-2} \text{ N m}^{-2}$  on average along the section and during the glider mission (inset in Fig. 1). The resultant velocity that would be associated with a return flow compensating the Ekman transport is

$$u_{\text{return}} = \frac{\tau^y}{\rho_0 f} \frac{1}{\delta_{\text{return}}}, \quad (1)$$

with  $f = -3.5 \times 10^{-5} \text{ s}^{-1}$  the Coriolis parameter and  $\rho_0 = 1026 \text{ kg s}^{-3}$  a reference density. Assuming that the return flow extends over  $\delta_{\text{return}} \sim 100 - 200 \text{ m}$ , the mass conservation would yield an averaged velocity of  $\sim 1 - 2 \text{ cm s}^{-1}$ . Cross-shore ADCP velocity at 100 m shows great variability. Averaged along the glider section between 50 and 100 km the mean value is  $\sim 1 \text{ cm s}^{-1}$  (rms  $\sim 1.3 \text{ cm s}^{-1}$ ), which is not significant but would also indicate the presence of a return flow. Subsurface geostrophic flow was estimated from ship CTD data around the glider section and thermal wind. The surface geostrophic flow from altimetry was used as reference velocity. This estimate of the geostrophic velocity confirms the presence of a coastward flow at 100 m albeit with a much larger magnitude ( $\sim 8 \text{ cm s}^{-1}$ ) during the whole deployment. Altogether, these estimates of the cross-shore velocity are certainly rough owing to the accuracy of the instrument or the method used. Nevertheless, they all suggest that a slow return flow could explain the coastward transport of the salinity anomalies.

## 5. Discussion

Small-scale filamentation of tracer in frontal zones has been observed several times, and previous studies related it to several dynamical mechanisms (Nandi et al. 2004;

Shcherbina et al. 2009, 2010). They can originate from self-driven, double-diffusive interleaving (Ruddick and Richards 2003) or from the broad range of processes known to create submesoscale lateral filamentation in frontal regions (Mahadevan and Tandon 2006): frontogenesis (Pollard and Regier 1992), nonlinear Ekman transport across fronts (Thomas and Lee 2005), and stirring of thermohaline gradients by mesoscale eddies (Smith and Ferrari 2009). These processes are known to occur simultaneously in the vicinity of oceanic density fronts (Capet et al. 2008a), and detailed quantitative analysis is needed to differentiate them. This is not achievable here with our dataset, particularly owing to the 2D nature of the glider data and the sparseness of the ship CTD stations. Nevertheless careful observation and scaling arguments can provide invaluable information on which mechanisms could be mainly responsible.

### a. Double diffusion

The presence of the relatively salty STSW over the fresher ESPIW makes the vertical distribution of salinity potentially favorable to double diffusion in the form of salt fingers (Schmitt 1994; St. Laurent and Schmitt 1998; Pastor et al. 2008). A good indicator of double diffusion is the Turner angle (Ruddick 1983)

$$\text{Tu} = \tan^{-1} \frac{\alpha \theta_z - \beta S_z}{\alpha \theta_z + \beta S_z}, \quad (2)$$

where  $\alpha$  is the thermal expansion coefficient and  $\beta$  the saline contraction coefficient. Regions where angles are greater than  $45^\circ$  (respectively inferior to  $-45^\circ$ ) are favorable to salt fingering (respectively diffusive convection) while regions where  $-45^\circ < \text{Tu} < 45^\circ$  are stable. Between 50- and 150-m depth, where the salinity intrusions are more pronounced, Turner angles greater than  $45^\circ$  are found for 25% of the data points, whereas fewer than 7% were less than  $-45^\circ$ . This means that the flow could be prone to salt fingering. However, double diffusion is usually characterized by regular-shaped thermohaline staircases (Kelley et al. 2003) that were not observed in the salinity or the temperature profiles despite the high vertical resolution ( $\sim 1 - 2 \text{ m}$ ) of our measurements. A Turner angle greater than  $45^\circ$  is a necessary but not sufficient condition, as double-diffusive interleaving can be enhanced or suppressed by baroclinicity. According to the linear stability analysis of May and Kelley (1997), the criterion for double diffusive interleaving is

$$\frac{1}{\rho_0} \frac{k}{m} \left( \bar{\rho}_x - \frac{k}{m} \bar{\rho}_z \right) - (1 - \gamma_f) \beta \frac{k}{m} \left( \bar{S}_x - \frac{k}{m} \bar{S}_z \right) < 0, \quad (3)$$

TABLE 1. Base state properties along the section.

Parameter	Min	Max	Avg
$\bar{S}_x$	$-2.26 \times 10^{-6}$	$1.96 \times 10^{-6}$	$-1.77 \times 10^{-7}$
$\bar{S}_z$	$-2.00 \times 10^{-3}$	$2.20 \times 10^{-3}$	$5.26 \times 10^{-4}$
$\epsilon_z \bar{S}_x / \bar{S}_z$	$-1.27 \times 10^{-4}$	$1.02 \times 10^{-4}$	$1.53 \times 10^{-5}$
$\bar{\rho}_x$	$1.26 \times 10^{-6}$	$1.10 \times 10^{-5}$	$5.17 \times 10^{-6}$
$\bar{\rho}_z$	$-9.60 \times 10^{-3}$	$-1.80 \times 10^{-3}$	$-4.60 \times 10^{-3}$
$\bar{\rho}_x / \bar{\rho}_z$	$-2.20 \times 10^{-3}$	$-6.30 \times 10^{-4}$	$-1.10 \times 10^{-3}$
$s^*$	$-2.10 \times 10^{-3}$	$-5.89 \times 10^{-4}$	$-1.03 \times 10^{-3}$

with  $-k/m$  the slope of the observed interleaving layers,  $\beta$  the contraction coefficient for salinity,  $\gamma_f$  the flux ratio for salt fingering ( $\gamma_f = 0.7$ , McDougall and Ruddick 1992),  $\bar{\rho}$  and  $\bar{S}$  the background state ( $x$  is the across front coordinate, subscripts  $x$  and  $z$  denote the horizontal and vertical partial derivatives respectively).

Introducing the quantity

$$\epsilon_z = -(1 - \gamma_f) \beta \bar{S}_z / (\bar{\rho}_z / \rho_0),$$

Eq. (3) implies that for double diffusion to occur the slope of the interleaving layers,  $|k/m|$ , has to be less than a critical slope  $|s^*|$ , defined by

$$s^* = \frac{\epsilon_z \bar{S}_x / \bar{S}_z + \bar{\rho}_x / \bar{\rho}_z}{\epsilon_z + 1}. \quad (4)$$

We define here the background state as a linear interpolation along the horizontal direction between a “coastal” profile and an “offshore” profile in the transition zone, as in Bianchi et al. (2002). The mean profiles were computed by averaging all glider profiles between 40–65 and 65–100 km, respectively. Because of the presence of the fresh ESPIW, the horizontal and vertical gradients of background salinity change sign at different depths (Table 1). Nevertheless, in our case,  $|\bar{\rho}_x / \bar{\rho}_z| > |\epsilon_z \bar{S}_x / \bar{S}_z|$ ,  $\bar{\rho}_x / \bar{\rho}_z < 0$ , and  $\epsilon_z > -1$ , so  $s^*$  is always negative and ranges between  $-2.1 \times 10^{-3}$  and  $-5.9 \times 10^{-4}$  (see Table 1). The slopes calculated from the sections (see section 4.b) are much greater and range from  $1.9 \times 10^{-3}$  to  $1.5 \times 10^{-2}$ . Note that our slope estimates are lower bounds as these features would appear less steep than in reality in case they also slope in a direction perpendicular to the glider section (see details in section 5c). Therefore, it is unlikely that the salinity intrusions may result from double diffusion.

### b. Secondary cross-frontal circulations

Fronts are regions where large vertical velocities can develop and have a local effect on the distribution of properties (Pollard and Regier 1992). Frontal subduction can drive thermohaline and biogeochemical fluxes from

the mixed layer to the ocean interior due to ageostrophic cross-frontal circulations associated with the meandering of a density front (Wang 1993; Spall 1995). Several studies have also investigated the influence of wind forcing on a density front (Lee et al. 1994; Thomas and Lee 2005; Mahadevan and Tandon 2006) and showed that downfront winds can intensify those ageostrophic cross-frontal circulations through nonlinear Ekman pumping/suction.

In a region rich in mesoscale eddies and meanders, it is likely that the horizontal deformation of the front plays an important role in driving vertical velocities. In quasigeostrophic theory, ageostrophic motion arise to restore the thermal wind balance that geostrophic motions with strain and shear tend to destroy. Ageostrophic vertical velocities associated to this mechanism can be estimated by the divergence of the  $\mathbf{Q}$  vector (Hoskins et al. 1978). Thus, on an  $f$  plane vertical velocity is forced solely by the divergence of the kinematic deformation, called the  $\mathbf{Q}$  vector:

$$\mathbf{Q} = (Q_1, Q_2) = \left( \frac{g}{\rho_0} \frac{\partial \mathbf{V}_g}{\partial x} \cdot \nabla \rho, \frac{g}{\rho_0} \frac{\partial \mathbf{V}_g}{\partial y} \cdot \nabla \rho \right), \quad (5)$$

where  $\mathbf{V}_g = (u_g, v_g)$  comprises the cross-shore and alongshore components of the geostrophic horizontal velocity. The ship CTDs provide a quasi-synoptic 3D mesoscale sampling ( $\sim 25$ -km horizontal resolution) around the glider section. Using geostrophic surface velocities derived from altimetry (AVISO), density from the ship CTDs, and thermal wind balance, both components of the mesoscale  $\mathbf{Q}$  vector can be estimated. Objective analysis using a Gaussian covariance function with spatial decorrelation scale of 25 km is used to produce maps of density and horizontal velocity on a uniform rectangular grid. The vertical velocity can then be diagnosed by the quasigeostrophic  $\omega$  equation (Hoskins et al. 1978):

$$N^2 \nabla_h^2 w + f^2 \frac{\partial^2}{\partial z^2} w = 2 \nabla \cdot \mathbf{Q}, \quad (6)$$

where  $N^2 = \partial b / \partial z$  is the square of the Brünt Väisälä frequency, with  $b = -(g/\rho_0)\rho$  the buoyancy. Solution of

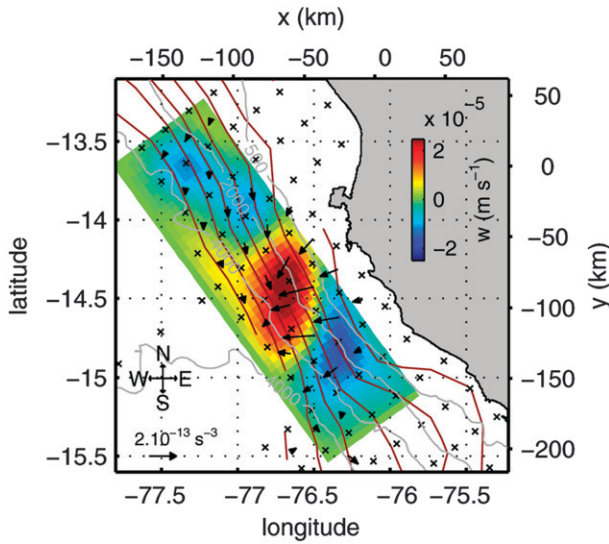


FIG. 9. Vertical velocity at 100 m from the  $\omega$  equation. Black arrows represent the  $\mathbf{Q}$  vector at 100 m estimated using geostrophic surface velocities derived from altimetry (AVISO) and density from the ship CTDs between 3 and 17 Oct. Black crosses indicate the position of the ship CTDs. Density contours (every  $4 \times 10^{-2} \text{ kg m}^{-3}$ ) are indicated with brown lines. Gray lines indicate the bathymetry.

the equation can be obtained by inverting the elliptic operator

$$L = N^2 \nabla_h^2 + f^2 \partial^2 / \partial z^2$$

and solving  $w = L^{-1} \cdot \nabla \cdot \mathbf{Q}$  (Giordani et al. 2006). The boundary condition is  $w = 0$  on all edges of the domain; thus the solution near the side and bottom boundaries should be viewed with caution (Rudnick 1996; Thomas et al. 2010).

Figure 9 displays the inferred vertical velocity at 100-m depth along with the  $\mathbf{Q}$  vector. An alternation of upward and downward velocities of  $\pm 2.5 \times 10^{-5} \text{ m s}^{-1}$  on both sides of the meandering front, with horizontal scales of  $\sim 50 \text{ km}$ , could drive vertical fluxes leading to thermo-haline intrusions. Even though the scales resolved by the sparse CTD data and satellite altimetry prevent us from concluding that the observed intrusions are linked with the kinematic deformation of the front, it appears to be an important process at stake in the region.

Another diagnostic for ageostrophic submesoscale circulations, which could give indications at smaller scale, is the potential vorticity (hereafter PV). It has been shown that in regions of low PV, for a given geostrophic forcing  $\nabla \cdot \mathbf{Q}$ , the vertical circulation is enhanced (Yoshikawa et al. 2001; Thomas et al. 2008). Besides, regions where the PV changes sign tend to relate with intense submesoscale activity (Mahadevan and Tandon 2006; Thomas et al.

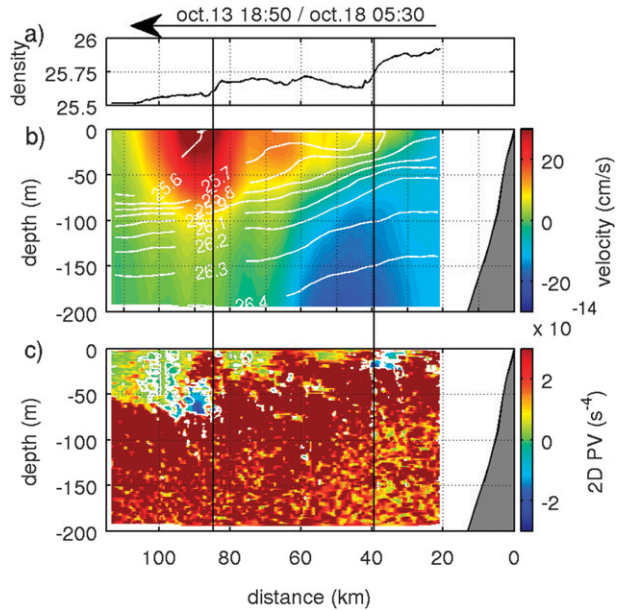


FIG. 10. (a) Cross-shore surface density profile, (b) absolute geostrophic velocity perpendicular to glider section #3 (color coded,  $\text{cm s}^{-1}$ ). Smoothed density contours are indicated by white lines. (c) 2D potential vorticity  $q$  (color coded,  $\text{s}^{-4}$ ) from glider section #3 with white contour corresponding to  $q = 0 \text{ s}^{-4}$ . Vertical black lines mark the position of the most pronounced surface density fronts.

2008). The geostrophic two-dimensional Ertel potential vorticity (Hoskins 1974), using the thermal wind balance, is computed as follows:

$$q_g = f \left( f + \frac{\partial v_g}{\partial x} \right) N^2 - f \frac{\partial v_g}{\partial z} \frac{\partial b}{\partial x} \approx f \left( f + \frac{\partial v_g}{\partial x} \right) N^2 - \left( \frac{\partial b}{\partial x} \right)^2, \quad (7)$$

The  $x$  axis is oriented cross shore, positive eastward, and the  $y$  axis is oriented alongshore, positive equatorward. Figure 10 shows an example of this computation for glider section #3. One can observe that the PV is almost zero in the mixed layer with large zones of negative PV located near the density fronts ( $z \sim 70 \text{ m}$ ,  $x \sim 90 \text{ km}$  and  $z \sim 25 \text{ m}$ ,  $x \sim 35 \text{ km}$ , Fig. 10c). Both regions of negative PV are located below strong horizontal gradients in the surface layer (Fig. 10a). Our PV estimates are  $q \sim -3.4 \times 10^{-14} \text{ s}^{-4}$  in a patch of  $\sim 3 \text{ km}$  width centered on  $90 \text{ km}$ , with  $dv/dx \sim -1.4 \times 10^{-7} \text{ s}^{-1}$ . Averaging the PV in a larger patch of  $\sim 10 \text{ km}$  width horizontally leads to  $q_g \sim -1.9 \times 10^{-14} \text{ s}^{-4}$ , which is still significant.

Another way to verify that inertial instability may occur, which is less sensitive to the errors that could be introduced by the derivatives, is to compare the slopes of absolute momentum ( $m = fx + v$ ) and buoyancy isolines (Thomas et al. 2010). Using  $m$  in Eq. (7) yields

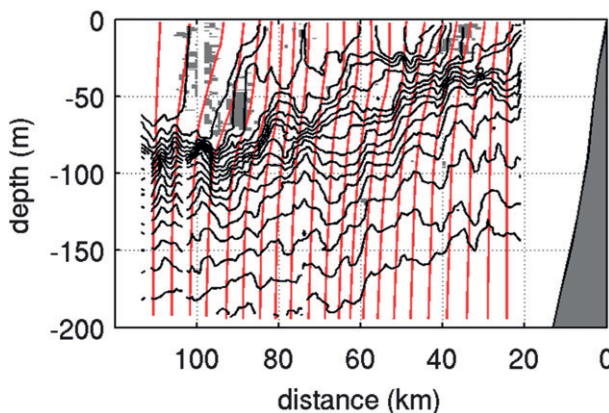


FIG. 11. Absolute momentum surface (red contours,  $\text{m s}^{-1}$ ) and density (black contours,  $\text{kg m}^{-3}$ ) for glider section #3. Contour intervals are  $0.15 \text{ m s}^{-1}$  for absolute momentum and  $5 \times 10^{-2} \text{ kg m}^{-3}$  for density. Zones of negative PV are marked in gray.

$$q = f \left( \frac{\partial m}{\partial x} \frac{\partial b}{\partial z} - \frac{\partial m}{\partial z} \frac{\partial b}{\partial x} \right). \quad (8)$$

Hence,  $q$  becomes negative when isolines of  $b$  are steeper than those of  $m$ . As shown in Fig. 11 for section #3, isolines of  $m$  are steeper than those of  $b$  almost everywhere except in the specific regions where negative PV patches were found.

Note that this estimate may be sensitive to the value of  $dv/dx$  in Eq. (7), which could be underestimated owing to the horizontal smoothing used to compute the geostrophic velocity. However, when considering hypothetically a much lower vertical vorticity ( $dv/dx = 2f \sim -7 \times 10^{-5} \text{ s}^{-1}$ ), the  $-(\partial b / \partial x)^2$  term in Eq. (7) still overcomes and the minimum of  $q_g$  in the patch remains negative. Potential vorticity from the glider measurements and from the ADCP were also compared at the crossing point of the ship and glider, and a mean difference of  $\sim 2.4 \times 10^{-14} \text{ s}^{-4}$  (rms  $\sim 2.2 \times 10^{-14} \text{ s}^{-4}$ ) was observed. However, the crossing point is located in a region of positive PV, which prevents us from validating our negative PV estimates with ADCP data.

Consequently, the PV has been estimated for the whole experiment. On each glider section (not shown) one or two patches of negative PV presenting horizontal and vertical scales of about  $\sim 5 \text{ km}$  and  $\sim 25 \text{ m}$ , respectively, can be observed in the mixed layer. This suggests that the flow is susceptible to inertial instability, which may drive submesoscale cross-frontal velocities.

The wind blowing in the direction of the frontal jet throughout the glider mission (see inset in Fig. 1) can be responsible for the very low PV in the mixed layer since it tends to extract PV from the surface (Thomas 2005). Such wind induces a transport of water perpendicular to

the frontal jet. Dense water is advected over lighter water, reducing the stratification and participating in the setting of ageostrophic secondary circulations (ASC) via symmetric instabilities (Paduan and Niiler 1990; Thomas and Lee 2005; Thomas 2005; Capet et al. 2008b). Those ASC feedback upon themselves and enable exchanges with deeper waters. Variation in the nonlinear Ekman transport (Stern 1965; Niiler 1969) results in nonlinear Ekman pumping/suction (Thomas and Rhines 2002). The associated vertical velocity is

$$w_{E_{nl}} = \frac{1}{\rho_0(f + \zeta)} \frac{\partial \tau^y}{\partial x} + \frac{\tau^y}{\rho_0(f + \zeta)^2} \frac{\partial \zeta}{\partial x}, \quad (9)$$

where  $\zeta$  is the surface vertical vorticity. Close to the surface front ( $x \sim 85 \text{ km}$  in glider section #3), strong density gradients and large variations in alongfront surface velocity are found. From the dense side to the light side of the front  $\zeta$  varies from  $\sim 2 \times 10^{-5} \text{ s}^{-1}$  to  $\sim -2.5 \times 10^{-5} \text{ s}^{-1}$ . Note that it corresponds to a local Ro  $\sim 0.5$  much larger than the one typical of the upwelling system (cf Section 3). The obtained velocity is  $w_{E_{nl}} \sim 0.1 \text{ cm s}^{-1}$  ( $\sim 86 \text{ m day}^{-1}$ ), which is coherent with previous estimates of the nonlinear Ekman pumping/suction (Mahadevan and Tandon 2006; Thomas et al. 2010). However the three-dimensional nature of the dynamics cannot be ignored, and this two-dimensional scaling can only provide an upper bound to characterize vertical velocities in the mixed layer in the frontal region.

ASC are usually considered as mostly affecting the mixed layer, and it is not clear how those intense vertical fluxes generated near the surface would influence the repartition of properties below the surface layer (Mahadevan and Tandon 2006; Thomas et al. 2010). Even if frontal vertical velocities could play a role in the formation of thermohaline intrusions, considering the subsurface location of the salinity tongues, other processes are certainly also at work here.

Concerning the surface repartition of biogeochemical properties, satellite images provide very little information due to significant cloud cover in this area or lack of horizontal resolution to study such small-scale features. Figure 1 displays the only useful satellite image (ocean color) that could be found over this region and during the glider deployment. It shows a chlorophyll-rich filament separated from the highly productive coastal area by a distance of 20–30 km. This filamentary structure was also sampled by the glider during section #9, showing a local surface chlorophyll maximum spanning from 60 to 80 km from the coast (Fig. 6c). The northern and southern extremities of the filament seem to swirl around eddies of  $\sim 50 \text{ km}$  diameter (C and A, respectively). However, a significant portion (at least

a third of the filament,  $\sim 100$  km alongfront) is located relatively far from the eddies (more than 1–2 diameters) so that they are unlikely to influence its dynamics there. This suggests that frontal vertical circulations could have a large alongfront extension and surface signature, which may be due to the action of large-scale atmospheric forcing on a relatively rectilinear upwelling front. However, we lack satellite observations and high-resolution in situ data north and south of the glider section to evaluate this hypothesis for the whole period of the experiment. We cannot rule out the possibility that this offshore filament may result from an upwelling event at the coast and has been advected westward then northward by the frontal jet.

### c. Mesoscale stirring by geostrophic turbulence

Along-isopycnal-compensated thermohaline intrusions can be driven by the mesoscale stirring of large-scale temperature and salinity gradients by geostrophic turbulence (Smith and Ferrari 2009). This process likely takes place in the Peru upwelling region because of the presence of mesoscale eddies (see mesoscale eddies in Fig. 1) and of the  $T$ – $S$  horizontal gradients between the offshore fresh ESPIW and nearshore saltier CCW (Fig. 5). In this case, Smith and Ferrari predict that geostrophic turbulence generates thermohaline filaments with aspect ratio of vertical to horizontal scales proportional to  $f/N$ . Estimates of the slopes of the filaments on a 40-m vertical scale (hereafter  $\hat{s}$ ) were carried out in section 4b. The value of  $N$  at 100-m depth and at the position of each intrusions was estimated. Figure 7 displays the slopes of the salinity intrusions superimposed with lines of slope  $f/N$  for glider sections #5 and #6. The lines with slope  $f/N$  are slightly steeper than the observed salinity tongues, except for one offshore structure ( $T_{fl}$ ). The same analysis has been carried out for each section, and for each identified saline filament. Here  $\hat{s}$  ranges from 0.2% to 1.5%, and  $f/N$  at 100 m from 0.3% to 1.2%. The slopes for all sections are compared in Fig. 12a. The observed slopes are scattered around the  $x = y$  line and most of them are situated below at about 0.2% – 0.6%. Six out of 30 values of  $\hat{s}$  are greater than  $f/N$  for values of  $f/N \sim 0.4\%$  – 0.6%. Despite the high degree of scatter, the center of the distribution is nearly on the  $x = y$  line ( $\hat{s} \sim 0.5$ ,  $f/N \sim 0.65$ ).

A similar diagnostic is provided by the probability density function (PDF) of the lateral and vertical salinity gradients along the section, whose structure can be compared with an average Prandtl ratio  $N/f$  [see Fig. 14 in Smith and Ferrari (2009)]. This gives a more quantitative insight on the scatter of the filament slopes about the mean  $N/f$ . The 2D PDF of  $(\partial S^2 / \partial z, \partial S^2 / \partial x)$  at 100 m in the transition zone are plotted in Fig. 12b, along with

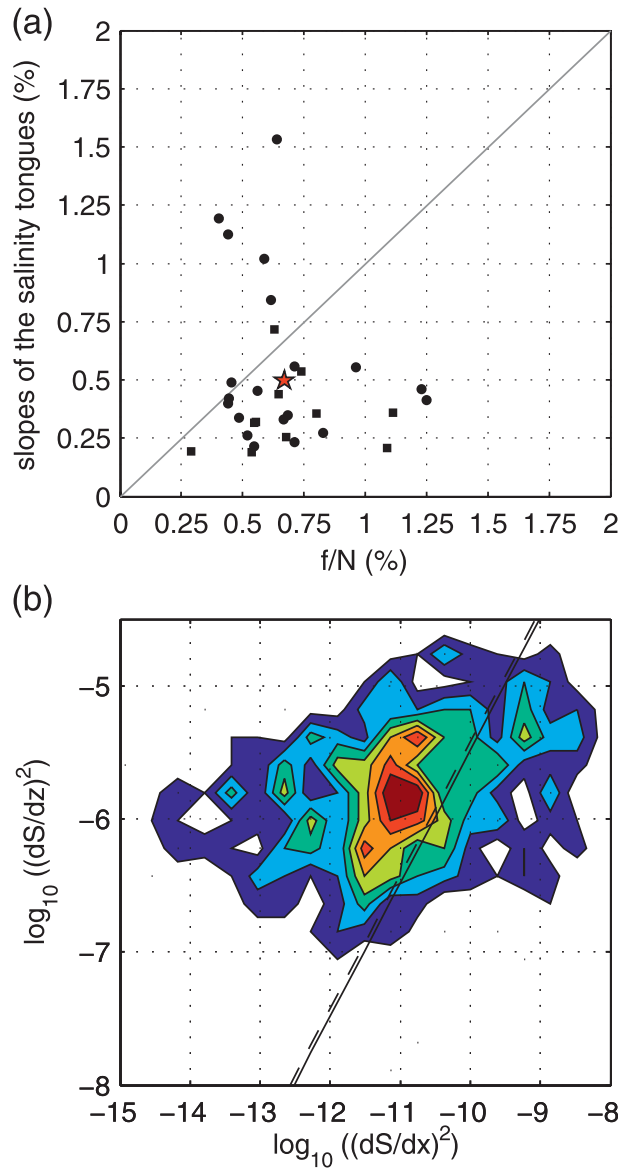


FIG. 12. (a) Comparison between  $f/N$  (calculated at 100-m depth) and slopes of the salinity structures (estimated from the local salinity minima and maxima at 120 and 80 m). Squares (circles) mark values from saline (freshwater) anomalies. The red star marks the center of mass of the distribution. (b) Probability distribution function of  $(\partial S / \partial z)^2$  and  $(\partial S / \partial x)^2$  at 100 m. The black line represents the slope  $(N/f)^2$  (calculated at 100-m depth) and the dashed line represents the slope of the median value of  $(\partial S / \partial z)^2 / (\partial S / \partial x)^2$ .

a line of slope  $(N/f)^2 \sim 3.3 \times 10^4$  with  $N$  computed at 100-m depth and then averaged in the transition zone (between 30 and 90 km from the coast). Median values of vertical and horizontal gradients of salinity yield  $(\partial S / \partial z)^2 / (\partial S / \partial x)^2$  which is very close to the averaged Prandtl ratio squared.

Note that the slopes of the structures are necessarily underestimated owing to the observational sampling. To

sample perfectly the slope of those isohaline surfaces, the glider trajectory would have had to be perfectly aligned perpendicular to them. If the glider section departs from that, the slope inferred from the glider measurements would necessarily be smaller than the real one. The displacement of the salinity structures by 3D turbulence could thus explain the dispersion below the  $x = y$  line. Besides, in Smith and Ferrari (2009) the mean horizontal gradient has no vertical structure. In the present case, the background salinity presents a rich vertical structure due to the different water masses in the region. [As shown analytically in Smith and Ferrari, vertical tracer gradient may increase the aspect ratio of the filaments in comparison with that of a tracer without mean vertical gradient, thereby explaining the dispersion above the  $x = y$  line.] This analysis thus suggests that the observed submesoscale features could be the result of the stirring by the mesoscale circulation, which have been described as prominent circulations in this region.

## 6. Conclusions

Our data provides a unique set of finescale measurements in the Peru–Chile upwelling system, for a continuous 2-month period at a very high resolution: more than one profile per km with a vertical resolution of 1–2 m for each section (200-m depth, 100 km and 5 days duration). This constitutes the first available benchmark, in the upper ocean and at this horizontal resolution, for numerical physical and biogeochemical models of the Peru–Chile upwelling system. Hydrography and the glider residual drifts allowed us to estimate “absolute” geostrophic velocities, which are in agreement with ADCP data and altimetry-derived surface velocities. From our results, the equatorward PCC has a maximum velocity of about  $30 \text{ cm s}^{-1}$  whereas the PCUC flows poleward with a maximum speed of about  $15 \text{ cm s}^{-1}$  near 150–200 m depth during a period of 2 months.

Cross-isopycnal submesoscale thermohaline and chlorophyll intrusions were observed below the mixed layer, between the coastal upwelling area and the open sea, throughout the whole glider mission. Several structures generally at a distance of  $\sim 20$ –40 km were observed on each section. These structures suggest that vertical fluxes could not only enhance phytoplankton growth due to upwelling of subsurface nutrients into the euphotic layer, but also decrease the surface biomass due to submesoscale downwelling, a noteworthy unexpected mechanism in a major upwelling system.

The potential physical processes that could generate them were then investigated. Negative PV patches observed in the mixed layer would suggest the potential occurrence of inertial instability and the development of

cross-frontal cells, driven by the wind continuously blowing downfront, which may reach depths below the mixed layer. In addition, we investigated the role of mesoscale horizontal deformation of the upwelling front using a three-dimensional complementary dataset from a ship survey. Even though this analysis did not allow us to characterize this process at the submesoscale, this mechanism could also drive vertical velocities explaining the observed intrusions. Finally, the typical cross-shore slope of the intrusions is  $O(f/N)$ . This is significantly steeper than the slopes characteristic of double-diffusive interleaving. This would rather indicate that the stirring by geostrophic turbulence of the mesoscale cross-shore gradients is a prominent mechanism. In conclusion, we speculate that the tracer intrusions may be due to some combination of (i) the straining of horizontal density gradients by geostrophic turbulence, (ii) symmetric instability, and (iii) frontogenesis. Only a complementary high-resolution three-dimensional survey—for instance with several gliders following parallel cross tracks simultaneously—would allow one to further quantify the contribution of the different submesoscale processes at work in this frontal region.

Our results show that sustained glider observations, via a single repeated section perpendicular to the slope (100 km in 4–5 days), provide invaluable insights on the submesoscale dynamics of the upwelling. We advocate this approach in general for the coastal ocean and would recommend deploying gliders continuously over the year along such a repeat section. This would allow one to further document the spatial and temporal variability of the striking frontal submesoscale processes as observed in our study.

Finally, this study demonstrates that the glider technology can now allow efficient monitoring parts of the ocean that are important at global scale, but characterized by a strong variability at relatively small scale. Many other areas require sampling at much better resolution than the Argo scale ( $\sim 300$  km,  $\sim 10$  days, Gould et al. 2004) typical of the Global Ocean Observing System capabilities with in situ measurements, for a better understanding of the global ocean, and we suggest it should be used more generally.

**Acknowledgments.** This work was supported by IRD and CNRS-INSU. The authors wish to thank four anonymous reviewers for their constructive and helpful comments. We thank X. Capet, B. L. Hua, Y. Morel, and F. Colas for fruitful discussions. We also thank the R/V *Olaya* crew and the technical staff of IMARPE. We are grateful to the Peruvian Coast Guard for recovery of the glider. The satellite Chlorophyll a data was kindly provided by H. Demarcq. The glider Pytheas was provided

by ENSTA ParisTech. Financial support was provided by EGO-COST Action ES0904, FP7 EU project JERICO, and ANR VMCS2008 PEPS project.

## REFERENCES

- Behrenfeld, M. J., and E. Boss, 2006: Beam attenuation and chlorophyll concentration as alternative optical indices of phytoplankton biomass. *J. Mar. Res.*, **64**, 431–451.
- Bianchi, A. A., A. R. Piolaa, and G. J. Collinoa, 2002: Evidence of double diffusion in the Brazil–Malvinas confluence. *Deep-Sea Res.*, **49**, 41–52.
- Brink, K. H., D. Halpern, A. Huyer, and R. L. Smith, 1983: The physical environment of the Peruvian upwelling system. *Prog. Oceanogr.*, **12**, 285–305.
- Capet, X., J. C. McWilliams, M. J. Molemaker, and A. F. Shchepetkin, 2008a: Mesoscale to submesoscale transition in the California Current system. Part I: Flow structure, eddy flux, and observational tests. *J. Phys. Oceanogr.*, **38**, 29–43.
- , —, —, and —, 2008b: Mesoscale to submesoscale transition in the California Current system. Part II: Frontal processes. *J. Phys. Oceanogr.*, **38**, 44–64.
- Chaigneau, A., A. Gizolme, and C. Grados, 2008a: Mesoscale eddies off Peru in altimeter records: Identification algorithms and eddy spatiotemporal patterns. *Prog. Oceanogr.*, **79**, 106–119.
- , O. Pizarro, and W. Rojas, 2008b: Global climatology of near-inertial current characteristics from Lagrangian observations. *Geophys. Res. Lett.*, **35**, L13603, doi:10.1029/2008GL034060.
- , G. Eldin, and B. Dewitte, 2009: Eddy activity in the four major upwelling systems from satellite altimetry (1992–2007). *Prog. Oceanogr.*, **83**, 117–123.
- Chavez, F., A. Bertrand, R. Guevara-Carrasco, P. Soler, and J. Csirkef, 2008: The northern Humboldt current system: Brief history, present status and a view towards the future. *Prog. Oceanogr.*, **79**, 95–105.
- Davis, R. E., C. E. Eriksen, and C. P. Jones, 2002: Autonomous buoyancy-driven underwater gliders. *Technology and Applications of Autonomous Underwater Vehicles*, G. Griffiths, Ed., Taylor and Francis, 37–58.
- Echevin, V., F. Colas, A. Chaigneau, and P. Penven, 2011: Sensitivity of the northern Humboldt current system nearshore modeled circulation to initial and boundary conditions. *J. Geophys. Res.*, **116**, C07002, doi:10.1029/2010JC006684.
- Enfield, D. B., 1981: Thermally driven wind variability in the planetary boundary layer above Lima, Peru. *J. Geophys. Res.*, **86** (C3), 2005–2016.
- Fischer, J., and M. Visbeck, 1993: Deep velocity profiling with self-contained ADCP. *J. Atmos. Oceanic Technol.*, **10**, 764–773.
- Giordani, H., L. Prieur, and G. Caniaux, 2006: Advanced insights into sources of vertical velocity in the ocean. *Ocean Dyn.*, **56**, 513–524, doi:10.1007/s10236-005-0050-1.
- Gould, J., and Coauthors, 2004: Argo profiling floats bring new era of in situ ocean observations. *Eos, Trans. Amer. Geophys. Union*, **85**, 19, doi:10.1029/2004EO190002.
- Gourdeau, L., W. S. Kessler, R. E. Davis, J. Sherman, C. Maes, and E. Kestenare, 2008: Seaglider: A long-range autonomous underwater vehicle for oceanographic research. *J. Phys. Oceanogr.*, **38**, 715–725.
- Hoskins, B. J., 1974: The role of potential vorticity in symmetric stability and instability. *Quart. J. Roy. Meteor. Soc.*, **100**, 480–482.
- , I. Draghici, and H. C. Davies, 1978: A new look at the  $\omega$ -equation. *Quart. J. Roy. Meteor. Soc.*, **104**, 31–38.
- Huyer, A., 1980: The offshore structure and subsurface expression of sea level variations off Peru, 1976/77. *J. Phys. Oceanogr.*, **10**, 1755–1768.
- , M. Knoll, T. Paluszkiewicz, and R. L. Smith, 1991: The Peru undercurrent: A study in variability. *Deep-Sea Res.*, **38** (Suppl. 1), S247–S271.
- Johnston, T. M. S., D. L. Rudnick, and E. Palls-Sanz, 2011: Elevated mixing at a front. *J. Geophys. Res.*, **116**, C11033, doi:10.1029/2011JC007192.
- Kelley, D. E., H. J. S. Fernando, A. E. Gargett, J. Tanny, and E. Özsoy, 2003: The diffusive regime of double-diffusive convection. *Prog. Oceanogr.*, **56**, 461–481.
- Lee, D.-K., P. Niiler, A. Warn-Varnas, and S. Piacsek, 1994: Wind-driven secondary circulation in ocean mesoscale. *J. Mar. Res.*, **52**, 371–396.
- Lentz, S. J., and D. C. Chapman, 2004: The importance of nonlinear cross-shelf momentum flux during wind-driven coastal upwelling. *J. Phys. Oceanogr.*, **34**, 2444–2457.
- Mahadevan, A., and A. Tandon, 2006: An analysis of mechanisms for submesoscale vertical motion at ocean fronts. *Ocean Modell.*, **14**, 241–256.
- May, B. D., and D. E. Kelley, 1997: Effect of baroclinicity on double-diffusive interleaving. *J. Phys. Oceanogr.*, **27**, 1997–2008.
- McDougall, T. J., and B. R. Ruddick, 1992: The use of ocean microstructure to quantify both turbulent mixing and salt-fingering. *Deep-Sea Res.*, **39** (11–12), 1931–1952.
- McWilliams, J. C., F. Colas, and M. J. Molemaker, 2009: Cold filamentary intensification and oceanic surface convergence lines. *Geophys. Res. Lett.*, **36**, L18602, doi:10.1029/2009GL039402.
- Nandi, P., W. S. Holbrook, S. Pearse, P. Páramo, and R. W. Schmitt, 2004: Seismic reflection imaging of water mass boundaries in the Norwegian Sea. *Geophys. Res. Lett.*, **31**, L23311, doi:10.1029/2004GL021325.
- Niiler, P. P., 1969: On the Ekman divergence in an oceanic jet. *J. Geophys. Res.*, **74**, 7048–7052.
- Paduan, J. D., and P. P. Niiler, 1990: A Lagrangian description of motion in northern California coastal transition filaments. *J. Geophys. Res.*, **95** (C10), 18 095–18 109.
- Pallàs-Sanz, E., T. M. S. Johnston, and D. L. Rudnick, 2010: Frontal dynamics in a California Current system shallow front. Part I: Frontal processes and tracer structure. *J. Geophys. Res.*, **115**, C12067, doi:10.1029/2009JC006032.
- Pastor, M. V., J. L. Pelegri, A. Hernandez-Guerra, J. Font, J. Salat, and M. Emelianov, 2008: Water and nutrient fluxes off northwest Africa. *Cont. Shelf Res.*, **28**, 915–936.
- Penven, P., V. Echevin, J. Pasapera, F. Colas, and J. Tam, 2005: Average circulation, seasonal cycle, and mesoscale dynamics of the Peru Current system: A modeling approach. *J. Geophys. Res.*, **110**, C10021, doi:10.1029/2005JC002945.
- Pollard, R. T., and L. A. Regier, 1992: Vorticity and vertical circulation at an ocean front. *J. Phys. Oceanogr.*, **22**, 609–625.
- Ruddick, B., 1983: A practical indicator of the stability of the water column to double-diffusive activity. *Deep-Sea Res.*, **30** (10A), 1105–1107.
- , and K. Richards, 2003: Oceanic thermohaline intrusions: observations. *Prog. Oceanogr.*, **56**, 499–527, doi:10.1016/S0079-6611(03)00028-4.
- Rudnick, D. L., 1996: Intensive surveys of the Azores front. 2. Inferring the geostrophic and vertical velocity fields. *J. Geophys. Res.*, **101** (C7), 16 291–16 303.
- , R. E. Davis, C. C. Eriksen, D. M. Fratantoni, and M. J. Perry, 2004: Underwater gliders for ocean research. *Mar. Tech. J.*, **38**, 48–59.

- Schmitt, R. W., 1994: Double diffusion in oceanography. *Annu. Rev. Fluid Mech.*, **26**, 255–285.
- Schneider, W., R. Fuenzalida, E. Rodriguez-Rubio, and J. Garcés-Vargas, 2003: Characteristics and formation of eastern South Pacific intermediate water. *Geophys. Res. Lett.*, **30**, 1581, doi:10.1029/2003GL017086.
- Shcherbina, A. Y., M. C. Gregg, M. H. Alford, and R. R. Harcourt, 2009: Characterizing thermohaline intrusions in the North Pacific subtropical frontal zone. *J. Phys. Oceanogr.*, **39**, 2735–2756.
- , —, —, and —, 2010: Three-dimensional structure and temporal evolution of submesoscale thermohaline intrusions in the North Pacific subtropical frontal zone. *J. Phys. Oceanogr.*, **40**, 1669–1689.
- Smith, K. S., and R. Ferrari, 2009: The production and dissipation of compensated thermohaline variance by mesoscale stirring. *J. Phys. Oceanogr.*, **39**, 2477–2501.
- Smith, R. L., 1981: A comparison of the structure and variability of the flow field in three coastal upwelling regions: Oregon, northwest Africa, and Peru. *Coastal Upwelling*, F. A. Richards, Ed., Amer. Geophys. Union, 107–118.
- Spall, M. A., 1995: Frontogenesis, subduction, and cross-front exchange at upper ocean fronts. *J. Geophys. Res.*, **100** (C2), 355–367.
- St. Laurent, L., and R. W. Schmitt, 1998: The contribution of salt fingers to vertical mixing in the North Atlantic tracer release experiment. *J. Phys. Oceanogr.*, **29**, 1404–1424.
- Stern, M. E., 1965: Interaction of a uniform wind stress with a geostrophic vortex. *Deep-Sea Res.*, **12**, 2543–2557.
- Strub, P., J. Mesias, V. Montecino, J. Ruttlant, and S. Salinas, 1998: Coastal ocean circulation off western South America. *The Sea: The Global Coastal Ocean*, A. Robinson and K. Brink, Eds., *Regional Studies and Syntheses*, Vol. 11, J. Wiley and Sons, 273–313.
- Testor, P., and Coauthors, 2010: Gliders as a component of future observing systems. *Proc. OceanObs09: Sustained Ocean Observations and Information for Society*, Vol. 2, Venice, Italy, ESA, WPP-306. [Available online at <http://www.oceanobs09.net/proceedings/cwp/cwp89/>.]
- Thomas, L. N., 2005: Destruction of potential vorticity by winds. *J. Phys. Oceanogr.*, **35**, 2457–2466.
- , and P. B. Rhines, 2002: Nonlinear stratified spin-up. *J. Fluid Mech.*, **473**, 211–244.
- , and C. M. Lee, 2005: Intensification of ocean fronts by downfront winds. *J. Phys. Oceanogr.*, **35**, 1086–1102.
- , A. Tandon, and A. Mahadevan, 2008: Submesoscale processes and dynamics. *Ocean Modeling in an Eddying Regime*, *Geophys. Monogr.*, Vol. 117, Amer. Geophys. Union, 17–38, doi:10.1029/177GM04.
- , C. M. Lee, and Y. Yoshikawa, 2010: The subpolar front of the Japan/East Sea. Part II: Inverse method for determining the frontal vertical circulation. *J. Phys. Oceanogr.*, **40**, 3–25.
- Viúdez, A., and M. Claret, 2009: Numerical simulations of submesoscale balanced vertical velocity forcing unsteady nutrient-phytoplankton-zooplankton distributions. *J. Geophys. Res.*, **114**, C04023, doi:10.1029/2008JC005172.
- Wang, D.-P., 1993: Model of frontogenesis: Subduction and upwelling. *J. Mar. Res.*, **51**, 497–513.
- Wood, R., and Coauthors, 2010: The VAMOS ocean-cloud-atmosphere-land study regional experiment (VOCALS-rex): Goals, platforms, and field operations. *Atmos. Chem. Phys. Discuss.*, **10**, 1–53, doi:10.5194/acpd-10-1-2010.
- Yoshikawa, Y., K. Akitomo, and T. Awaji, 2001: Formation process of intermediate water in baroclinic current under cooling. *J. Geophys. Res.*, **106** (C1), 1033–1051.